Geophysical Journal International

Geophys. J. Int. (2021) **227,** 617–631 https://doi.org/10.1093/gji/ggab236
Advance Access publication 2021 June 21
GJI Geomagnetism, Rock Magnetism and Palaeomagnetism

Using magnetic techniques to calibrate hydrocarbon migration in petroleum systems modelling: a case study from the Lower Tertiary, UK Central North Sea

S.A. Badejo, A.R. Muxworthy, A. Fraser, M. Neumaier, J.R. Perkins, G.R. Stevenson and R. Davey

Department of Earth Science and Engineering, Imperial College London, London SW7 2BP, UK. E-mail: adrian.muxworthy@imperial.ac.uk

Accepted 2021 June 16. Received 2021 June 15; in original form 2021 January 4

SUMMARY

Magnetic minerals form or alter in the presence of hydrocarbons, making them a potential magnetic proxy for identifying hydrocarbon migration pathways. In this paper, we test this idea by magnetically measuring core samples from the Tay Fan in the Western Central Graben in the Central North Sea. In a companion paper, 3-D petroleum systems modelling has been carried out to forward model migration pathways within the Tay Fan. Rock magnetic experiments identified a range of magnetite, maghemite, iron sulphides, siderite, goethite and titanohematite, some of which are part of the background signal, and some due to the presence of hydrocarbons. Typical concentrations of the magnetic minerals were ∼10–200 ppm. Importantly, we have identified an increasing presence of authigenic iron sulphides (likely pyrite and greigite) along the identified lateral hydrocarbon migration pathway (east to west). This is likely caused by biodegradation resulting in the precipitation of iron sulphides, however, though less likely, it could alternatively be caused by mature oil generation, which subsequently travelled with the migrating oil to the traps in the west. These observations suggest mineral magnetic techniques could be a rapid alternative method for identifying the severity of biodegradation or oil maturity in core sample, which can then be used to calibrate petroleum systems models.

Key words: Europe; Environmental magnetism; Magnetic mineralogy and petrology; Rock and mineral magnetism.

1 INTRODUCTION

Previous studies have suggested low-altitude aeromagnetic surveys may be a complimentary method to conventional exploration techniques in remote areas (Donovan *et al.* 1984). These studies related the presence of short-wavelength magnetic anomalies to migration (or seepage) of hydrocarbons from reservoirs below. Hydrocarbons are known to cause reducing conditions at shallow depths that can chemically alter iron-bearing minerals to form authigenic iron oxides and/or sulphides (Reynolds *et al.* 1990; Burton *et al.* 1993). These iron minerals are sometimes ferromagnetic (*sensu lato*) like magnetite, pyrrhotite and greigite, though they can also be non-ferromagnetic such as pyrite and siderite (Costanzo-Alvarez *et al.* 2000; Aldana *et al.* 2011; Emmerton *et al.* 2013a; Badejo *et al.* 2021b). The resulting balance of iron-rich minerals is dependent on the local environment, which can lead to both positive or negative magnetic anomalies or no change in contrast (McCabe *et al.* 1987; Elmore *et al.* 1993). It is also possible, though less likely, that rather than hydrocarbon-induced diagenesis, the magnetic minerals found in reservoir core simply migrate with the hydrocarbon. Abubakar *et al.* (2015) experimentally demonstrated that fine grained (<50 nm) magnetite, greigite and pyrrhotite form in the oil kitchen, would be small enough to travel with the oil through the pore throats of shales, carrier beds and reservoir (Nealson 2009). Laboratory measurements under controlled conditions by Badejo *et al.* (2021b) suggest this mechanism may be possible.

It is clear that the presence of hydrocarbons alters the magnetic signature of the background rock. This alteration has the potential to map hydrocarbon migration and accumulation in the reservoir (Liu *et al.* 2006). In an earlier study, Abubakar *et al.* (2020) attempted to use mineral magnetic techniques to identify migration pathways in the Wessex Basin, UK, however, the tectonic history of the Wessex Basin is very complicated, and the magnetic findings were not entirely conclusive. The aim of this study was to better understand the link between hydrocarbon migration and magnetic mineralogy by examining an area with a relatively simple, well constrained geology. For this purpose, this paper concentrates on the Tertiary Tay fan in the Western Central Graben, North Sea, UK. The Tay Sandstone Member (TSM) was selected for the following reasons: (1) the TSM is not deformed (other than some gentle salt doming), and is laterally continuous with long-distance lateral migration of up to 50 km for oil and 32 km for gas (Cayley 1987), (2) the TSM is a high quality reservoir with high porosity and permeability (Banner *et al.* 1992), (3) high quality 3D seismic data is available over most of the study area and (4) there are a high number of wells in the area with good core coverage.

3-D petroleum systems and basin modelling of the Western Central Graben were carried out in a companion paper Badejo *et al.* (2021a). Through this modelling, Badejo *et al.* (2021a) identified hydrocarbon migration pathways in the TSM. Some of the observations in this paper aided the construction of the 3-D model; this is explained in section 5.3.

2 GEOLOGY OF THE CENTRAL NORTH SEA

Core samples were obtained from 18 hydrocarbon wells, three oil-show wells (containing non-commercial quantity of oil) and one dry well in the Central North Sea (CNS, Fig. 1). Well stratigraphy was cross-correlated using lithostratigraphy and 3-D seismic data (Badejo 2019; Badejo *et al.* 2021a).

The geology of the Central North Sea has been described in great detail by several authors (Cayley 1987; Isaksen 2004) and is very briefly summarized here. The Upper Jurassic Kimmeridge Clay is the main source rock in the area (Fig. 2). It is mature for oil to the east of the study area, with burial depths >3250 m and generally late mature for oil to early mature for gas at the eastern edge with burial depths of ∼4750 m (Barnard & Bastow 1991; Isaksen 2004). In the Central Graben the main hydrocarbon reservoirs are Upper Jurassic sandstones and Tertiary sandstones. The Upper Jurassic play (Fig. 2) is generally defined by two contrasting reservoirs: coastal-shelf sandstones (Fulmar Formation) and submarine-fan sandstones (Heather Formation), while the Tertiary play (Fig. 2) is defined by submarine-fan sandstones of the Forties Sandstone Member and TSM (Cayley 1987).

Initial accumulation of oil was in the Upper Jurassic Fulmar sandstones. As the source rock lies directly above this formation, Fulmar sandstones are ideal for short distance migration, however, the Fulmar is affected by both stratigraphic complexity and salt movement resulting in it being discontinuous and fractured. Over time sediment loading and compaction disequilibrium led to overpressure which triggered capillary failure in the seal above the Fulmar sandstones. This initiated vertical migration, with the fractured chalk and the salt wall and diapirs acting as a vertical conduits for migration into the overlying Tertiary sandstones (Badejo *et al.* 2021a). Badejo *et al.* (2021a) showed injectites (originating from the Forties Sandstone member and Maureen Formation) and salt diapirs are important vertical migration pathways into the TSM. All the core samples studied are from the TSM. Compared to the Fulmar sandstones the Tertiary sandstones are only slightly deformed and laterally continuous, facilitating lateral migration of distances of up to 50 km for oil and up to 32 km for gas (Cayley 1987; Badejo *et al.* 2021a). Up to 2750 m of uncompacted Eocene mudstones serve as the regional seal (Cayley 1987).

3 METHODOLOGY

3.1 Sample collection

Cores were sampled from the British Geological Survey (BGS) core repository in Keyworth, UK. Wire-line logs were initially used to identify the presence of gas and/or oil in the Tay sandstones (Fig. 2). At the BGS core repository samples were selected based on geological observation, that is water wet sandstone, oil-stained sandstone, siltstones and shale. Samples taken were typically 2 cm chips. A total of 188 samples were collected from 22 wells (Fig. 1, Table 1). Most of sandstones were very fine to fine grained, with very little sedimentary structures (Badejo 2019).

3.2 Magnetic measurements

A suite of magnetic measurements was carried out to determine the morphology, mineralogy and size of the magnetic minerals present; no single magnetic measurement yields a full description of the magnetic minerals. Room-temperature (RT) magnetic hysteresis measurements including first-order reversal curves (FORC) diagrams (Roberts *et al.* 2000), were made using a Princeton Measurements Vibrating Sample Magnetometer (VSM) at Imperial College. Magnetic hysteresis and FORC measurements help in the identification of domain state, grain size and aid in mineral identification. FORC diagrams are particularly diagnostic in isolating signals from different domain states in complex natural assemblages.

To aid magnetic mineralogy identification and the presence of very fine magnetic particles, we made low-temperature (LT, 20–300 K) experiments using a Quantum Design Magnetic Properties Measurement System (MPMS) at the Institute for Rock Magnetism (University of Minnesota). Some magnetic minerals have well-defined crystallographic transitions, for example the Verwey transition in magnetite at $T_V \sim 120$ K (Verwey 1939). Low-temperature measurements also help to identify fine grains (<30 nm) that are thermally activated at room-temperature, that is superparamagnetic grains, which are hard to identify at room-temperature as they are 'magnetically transparent'. By cooling the samples to very low temperatures (<30 K), such grains can be easily measured. To further identify the magnetic mineralogy of the samples, we measured high-temperature magnetic susceptibility curves to determine Curie temperatures. To do this we used an Agico KLY-2 Kappabridge susceptibility meter at Imperial College. Susceptibility was measured as samples were heated from room temperature to 700 °C in an argon atmosphere.

3.3 Scanning electron microscopy

To aid in the characterization of the magnetic minerals, we conducted scanning electron microscopy (SEM) combined energy dispersive X-ray (EDX) analysis on a Zeiss LEO Gemini 1525 at Imperial College. SEM imaging is particularly important for differentiating between—usually—detrital pyrrhotite and authigenic greigite, which have very different morphologies, but similar magnetic behaviour during magnetic hysteresis when a maximum field of only ∼1 T is available (Roberts *et al.* 2014). As the abundance of magnetic minerals was less typically $<<0.001$ per cent, magnetic extraction was needed before imaging (Emmerton *et al.* 2012; Emmerton *et al.* 2013b). Samples were crushed to an even grain size (∼50 µm), and passed through a Frantz electromagnet magnetic separator three times following the protocol developed by Chang

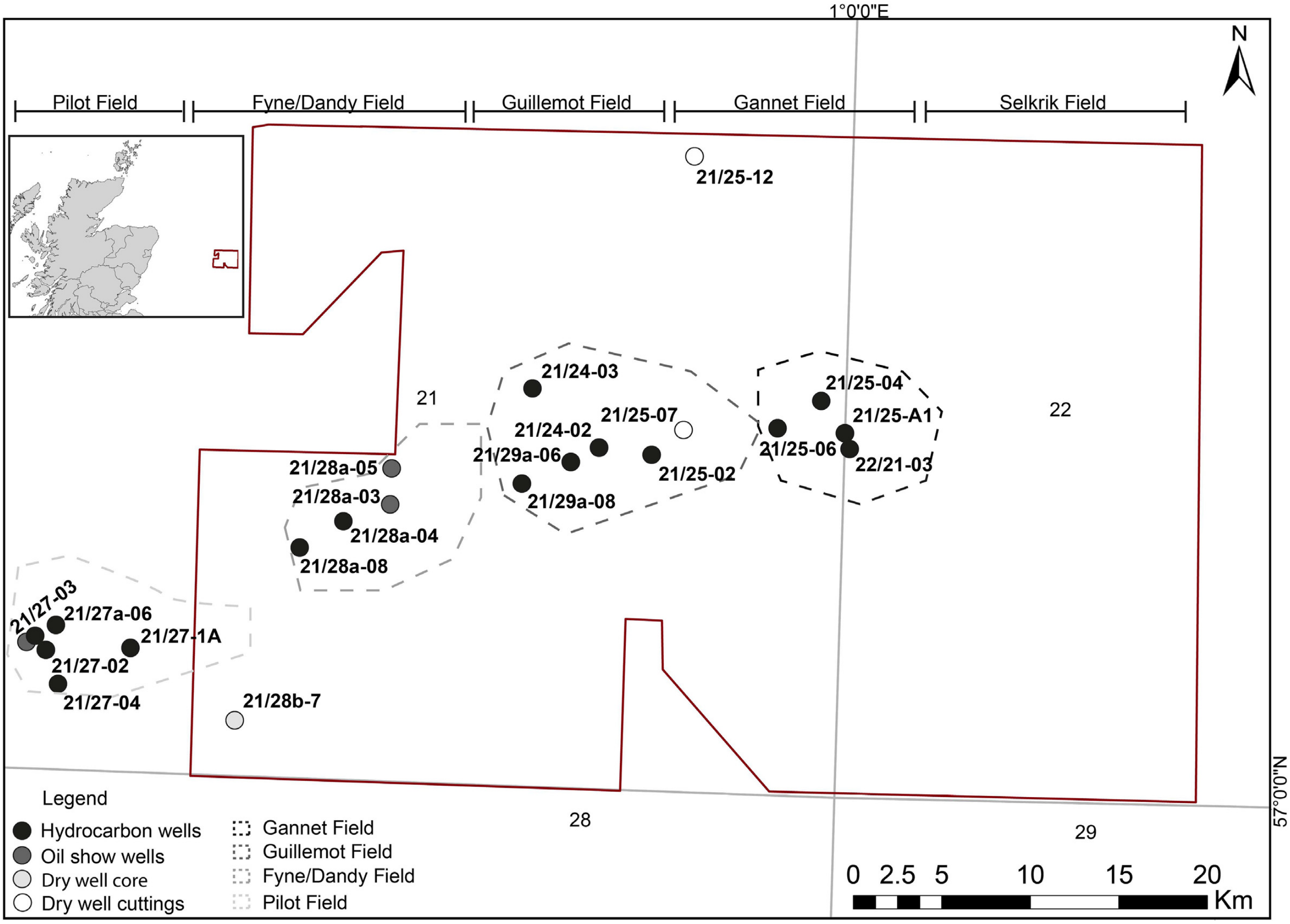

Figure 1. Location of the study area, showing the well numbers and relative locations. The study was undertaken with cores from 19 oil/gas wells, one dry well and cuttings from two dry wells. The polygon represents the 3-D seismic data available studied in the companion paper Badejo *et al.* (2021a) and Badejo (2019). The study area relative to Scotland, UK, is shown in the inset.

et al. (2012). Samples were ground and coated in gold for EDX analysis; the EDX had a spot size of ∼1 µm

3.4 Geochemical experiments

Some geochemical experiments were undertaken to determine if the dry core samples had ever been impregnated with oil. Samples from dry wells may appear water wet, but it is possible that oil has migrated through this area and the oil subsequently replaced by water, however, the oil could leave behind some organic residue (residual oil) in the samples that can still be extracted (Peters *et al.* 2006).

Core samples s70402, s70403 and S70404 from dry well 21/28b-07 were selected for column chromatography (Rowland & Revill 1995). Organic extraction was carried out before column chromatography. To do this a dichloromethane (DCM) and methanol (97:3) were added to the ground samples (5–10 g). The mixture was sonicated for 5 min then placed in a centrifuge at 1500 rpm for a further 5 min. The process was repeated until the solvent was clear. A rotary evaporator was used at 50 °C to increase the concentration of organic extracts in the solvent. This was left to dry leaving behind organic matter extracts. Aliphatic and aromatic constituents were extracted in the following way: (1) Alumina was activated in an oven for 1 hr at 150 °C, (2) the column was plugged with the activated alumina and small amounts pre-extracted using quartz wool, (3) small amounts of pre-extracted quartz wool were added to the sample vial, stirred with a clean spatula and left to dry; the dry mixture was added to the top of the column, (4) hexane was used to elute the aliphatic fraction while DCM was used to elute the aromatic fraction, and the fractions were collected in a test tube, (5) the fractions were reduced to <1 ml under a stream of nitrogen, (6) fractions were transferred into clean vials and allowed to dry and (7) the fractions were placed in a Gas Chromatography–Mass Spectrometer (GC-MS) for compound detection and identification.

4 RESULTS

4.1 Magnetic measurements

To summarize the range of behaviour from the 188 samples collected from 22 wells, we consider three oil producing wells 21/29a-08, 21/28a-03 and 21/24-03 (Figs 3–5) and one dry well 21/28b-07 (Fig. 6). The magnetic data are summarized at well level in Table 1.

4.1.1 Hysteresis and FORC analysis

Mass-normalized room-temperature hysteresis loops and susceptibility were measured for all samples; mean and median of measures

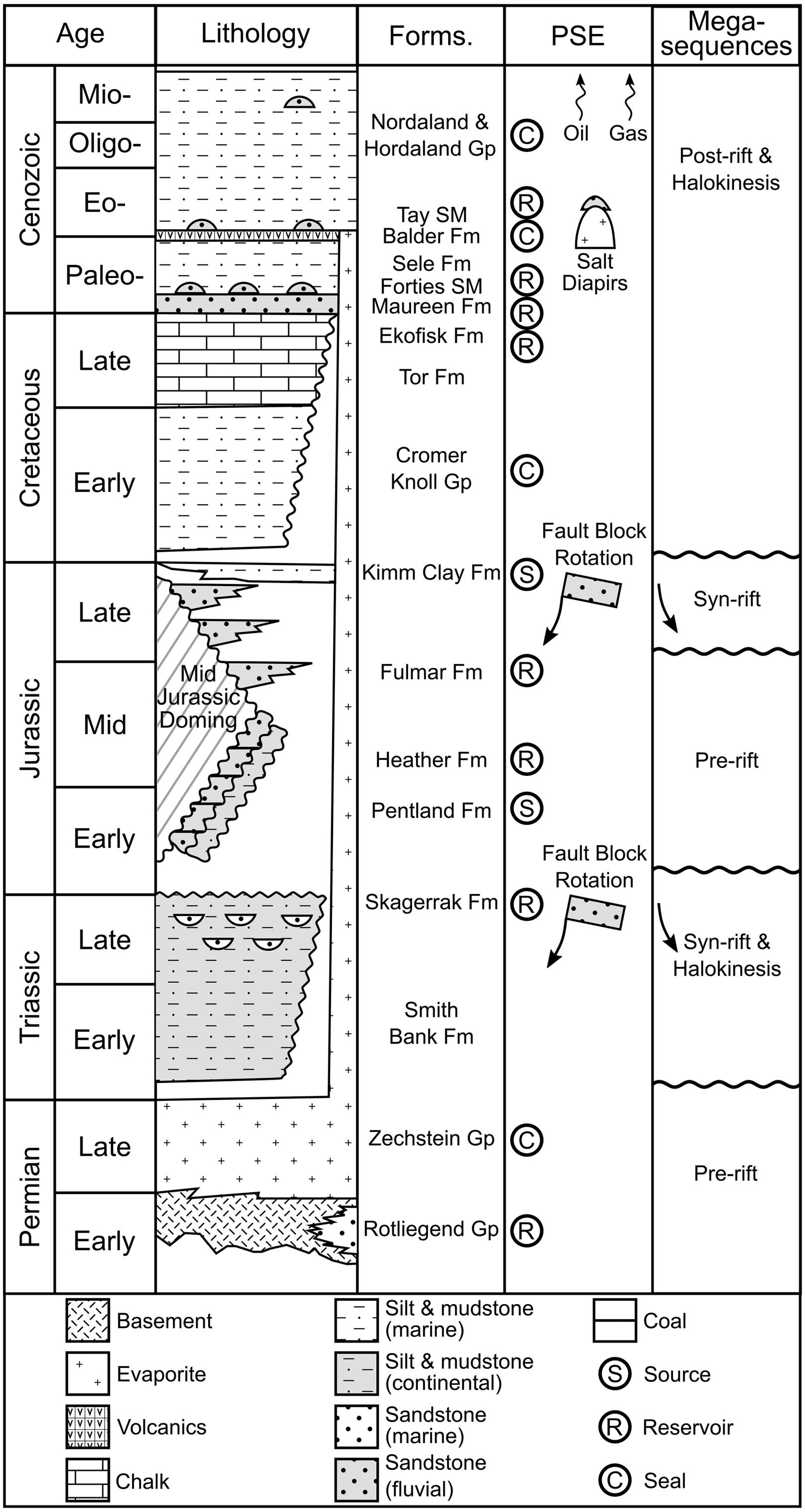

Figure 2. Generalized Central North Sea stratigraphic column showing depositional facies, tectonic history, source rock, possible reservoirs, seal and timing of hydrocarbon migration. Useful stratigraphic/seismic horizons are identified.

saturation magnetization (M_s), remanent saturation magnetization (M_{rs}), coercive force (B_c) and mass susceptibility values of all the wells used in this study are shown in Table 1. The hysteresis loops for all 188 samples were measured, and 110 FORC diagrams were measured. Some samples were too weak magnetically to measure FORC data, which required taking the mixed-second derivative of the data; no FORC data were measured for wells 21/29a-08 and 21/28-05 (Table 1). The samples were generally weak and most of the hysteresis loops had a low signal-to-noise ratios with a strong paramagnetic behaviour. M_s, M_{rs} and B_c are similar to the values Emmerton *et al.* (2013b) observed for oil stained and oil-free samples from Colombia, Canada, Indonesia and UK. Measured M_s,

Table 1. Mean and median of measured saturation magnetisation (M_s), remanent saturation magnetisation (M_{rs}), coercive force (B_c) and mass susceptibility (χ) for wells in the study area. All measured sample types are included in the calculation as the samples in the gas cap, oil-stained samples, water wet samples and siltstones typically have similar values. Hydrocarbon wells are roughly arranged from east to west. Note: The last 3 wells in italics are dry. Only well 21/28b-07 is cored, the other two wells (21/25-11 and 21/25-12) are cuttings.

Field	Well	Number of samples	Median M_s (10^{-3} Am^{2}kg^{-1})	Median M_{rs} (10^{-3} Am^{2}kg^{-1})	Median B_c (mT)	Median χ (10^{-3} m^{2}kg^{-1})	Main magnetic minerals
Gannet	21/25-04	16	1.0	0.2	8.8	1.1	magnetite, siderite
Gannet	22/21-03	9	8.3	1.1	8.1	15.2	magnetite, siderite
Gannet	21/25-A1	15	0.9	0.1	7.0	0.1	magnetite, siderite
Gannet	21/25-06	24	1.0	0.1	7.6	3.8	magnetite, siderite
Guillemot	21/25-02	6	1.3	0.1	14.9	13.9	magnetite, siderite
Guillemot	21/24-02	7	1.2	0.2	17.0	0.1	magnetite, siderite
Guillemot	21/24-03	11	2.0	0.3	11.0	0.2	magnetite, iron sulphides
Guillemot	21/29a-08	9	1.5	0.1	10.4	28.3	magnetite, siderite
Guillemot	21/29a-06	8	0.3	0.1	14.2	0.0	magnetite, siderite, iron sulphides
Fyne & Dandy	21/28a- 05	6	1.0	0.1	6.9	1.4	magnetite, siderite, iron sulphides
Fyne & Dandy	21/28a- 03	7	2.6	0.4	11.7	21.3	magnetite, siderite, iron sulphides
Fyne & Dandy	21/28a- 04	8	1.0	0.1	12.4	3.3	magnetite, siderite, iron sulphides
Fyne & Dandy	21/28a- 08	8	1.8	0.4	13.1	10.0	magnetite, siderite, iron sulphides
Pilot	21/27-1A	8	4.5	0.6	8.4	6.9	magnetite, siderite, iron sulphides
Pilot	21/27-04	16	1.1	0.2	15.9	5.5	magnetite, iron sulphides
Pilot	21/27a-05	4	1.0	0.0	13.8	5.7	magnetite, iron sulphides
Pilot	21/27-02	4	3.2	0.4	7.2	4.3	magnetite, iron sulphides
Pilot	21/27-03	7	0.9	0.1	10.9	1.2	magnetite, iron sulphides
Pilot	21/27a-06	7	1.7	0.3	11.0	0.1	magnetite, iron sulphides
Dry (Guillemot)	*21/28b-07*	5	1.6	0.3	15.8	0.2	magnetite, siderite
Dry	*21/25- 12*	5	6.6	0.8	10.9	1.5	magnetite
Dry	*21/25- 11*	5	10.2	1.2	8.8	7.5	magnetite

M_{rs} and mass susceptibility values cannot be used to consistently distinguish the four different rock types, that is oil-stained sandstone, water-wet sandstone, sandstone in the gas cap and siltstone, as they have similar values; however, the siltstones sometimes have much higher M_s, M_{rs} and mass susceptibility values compared to the other rock types. There is no significant difference in B_c for the different sample types within a well, suggesting similar magnetic mineralogies and grain size distributions, or the insensitivity of this parameter.

FORC diagrams for most of the samples suggest the presence of thermally relaxing single-domain (SD) particles as shown in s65297 (Fig. 4c). The presence of SD grains was identified by a peaked FORC distribution on the $B_i = 0$ axis or areas of negative values adjacent to the vertical axis (Roberts *et al.* 2000) as shown in s65301, s72417 and s72420 (Figs 4b, 5a and c). Samples with multiaxial anisotropy were identified by the steeply dipping negative region to the right of the B_u axis (Harrison & Lascu 2014; Valdez-Grijalva & Muxworthy 2019) as seen in s65301, s72420 and s72423 (Figs 4b, 5c and d). This feature may also be due to pseudo-SD (PSD) behaviour (Carvallo *et al.* 2003; Valdez-Grijalva *et al.* 2018). FORC diagrams for some samples have contours that diverge away from the origin, which also suggests the presence of PSD grains (Roberts *et al.* 2000) as seen in s65294 and s72417 (Figs 4a and 5a).

4.1.2 Low-temperature measurements

The following low-temperature sequences were carried out on the samples to identify possible magnetic transitions and nanometric magnetic minerals: (1) Low-temperature cycling—the samples were induced with a saturation isothermal remanent magnetisation (SIRM) at room-temperature (RTSIRM; field = 2.5 T), and then cooled to 10 K and back to 300 K in zero-field. This generates two curves called RTSIRM cooling and RTSIRM warming curves, respectively. (2) Field cooled (FC) and zero-field cooled (ZFC) warming curves—the samples were induced with an SIRM at 10 K and warmed in zero field to 300 K. In the ZFC scenario the sample is first cooled to 10 K in zero field, in the FC scenario in a field a 2.5 T. Low-temperature data were collected for 165 samples out of the 188 studied.

We interpreted the low-temperature curves using a range of criteria: (1) A discontinuity in the magnetic remanence at ∼120 K in the cycling cooling curves was observed in many of the samples and indicates the presence of magnetite (Figs 3–6); there was evidence for magnetite in most of the samples as has been reported previously (Elmore *et al.* 1993; Guzmán *et al.* 2011). (2) A 'hump' was observed in some of the cycling cooling curves, for example samples s72392 and s65300 (Figs 3b and 4d), which was interpreted as being indicative of the presence of maghemite (Özdemir & Dunlop 2010). (3) A pronounced drop in remanence between 10 and 40 K in the FC experiment was used to identify the presence of siderite as seen in samples s72392 and s65297 (Figs 3a and 4c). Siderite is paramagnetic at room temperature, but in the presence of a field during cooling it acquires a large thermoremanence below its Néel temperature (∼37 K) (Jacobs 1963). In common with magnetite, siderite was observed in many oil-core samples, for example s72392 and s65297 (Fig 3a and 4c). Some of the samples displayed measurement artefacts due to the 'zero-field' state in the MPMS not always being truly nulled during zeroing. This trapped field is two to three times the Earth's field; because the 'zero-field' state is non-zero, this can lead to a noticeable anomaly in remanence at 40 K in samples with high concentrations of siderite, for example, samples s63651 and s72392 (Figs 3a and b). (4) The increase in remanence on cooling in samples s63651, s65294, s65297 (Figs 3a, 4a and c) and in the dry well core (Fig. 6) suggests the presence of goethite or titanohematite (Rochette & Fillion 1989; Sprain *et al.* 2016). To definitively identify goethite, a goethite test was carried out using the protocol designed by Guyodo *et al.* (2006). Goethite tests showed

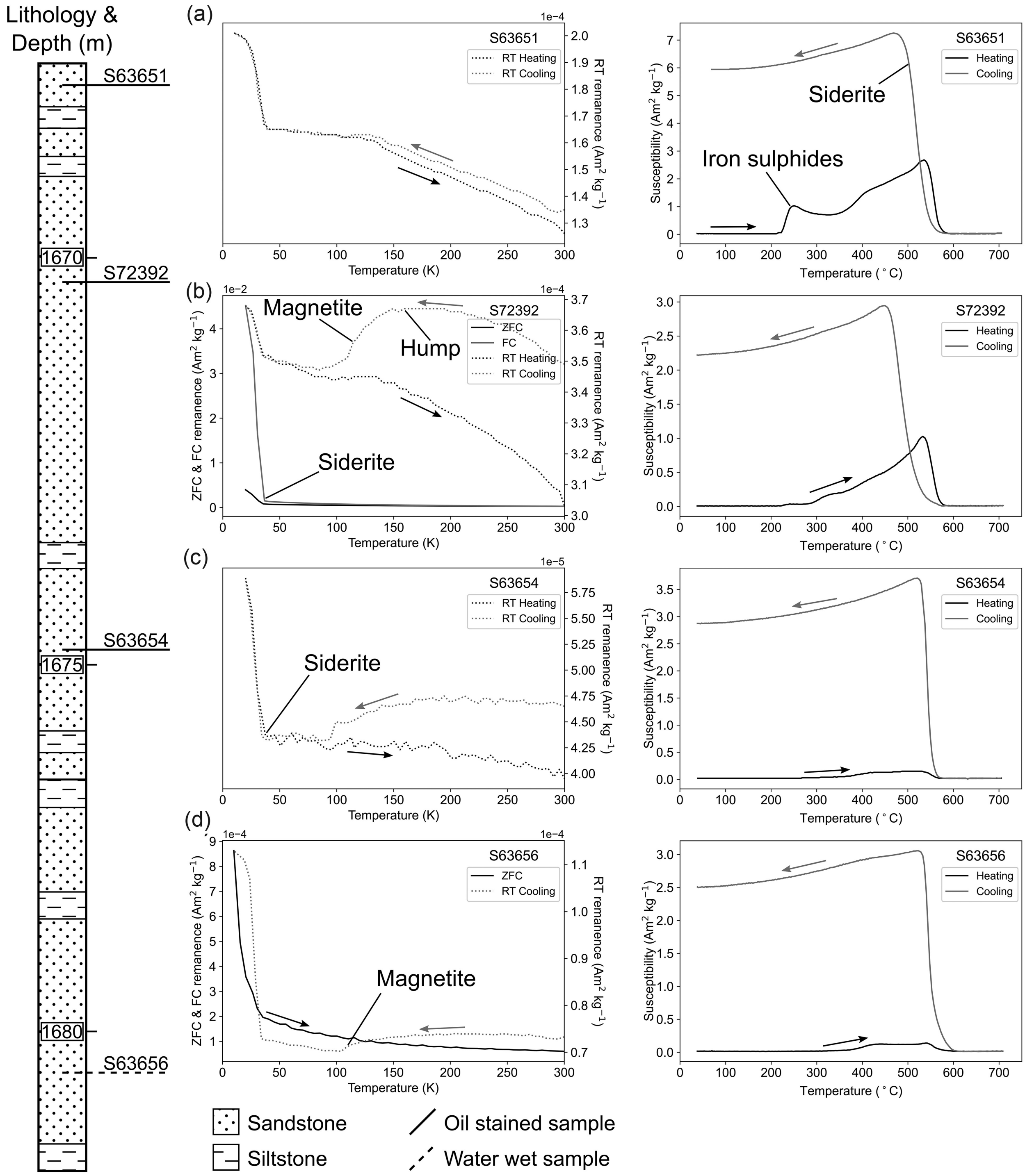

Figure 3. Representative samples from well 21/29a-08 (oil) showing the magnetic data (low-temperature magnetometry and high-temperature susceptibility (heated in Ar)) for four samples: (a) s63651, (b) s72392, (c) s63654 and (d) s63656. Data for s63651 and s72392 suggests the presence of siderite, magnetite and iron sulphides. s63654 and s63656 contains only siderite and magnetite.

a drop in remanence at room temperature suggesting some of the remanence is carried by goethite (Badejo 2019), but the continued increase in remanence on cooling suggests the presence of another high coercivity magnetic minerals with no low-temperature transition, likely titanohematite (Sprain *et al.* 2016). These two minerals have never been observed in studies carried out on samples from or near hydrocarbon wells, so they have been classed as background magnetic signals, that is not due to the reducing environment caused by hydrocarbons.

Monoclinic pyrrhotite's Besnus (∼34 K) transition (Besnus & Meyer 1964) was identified in only oil-showing well sample, that is s65300 (Fig. 4d), albeit from a water wet section,

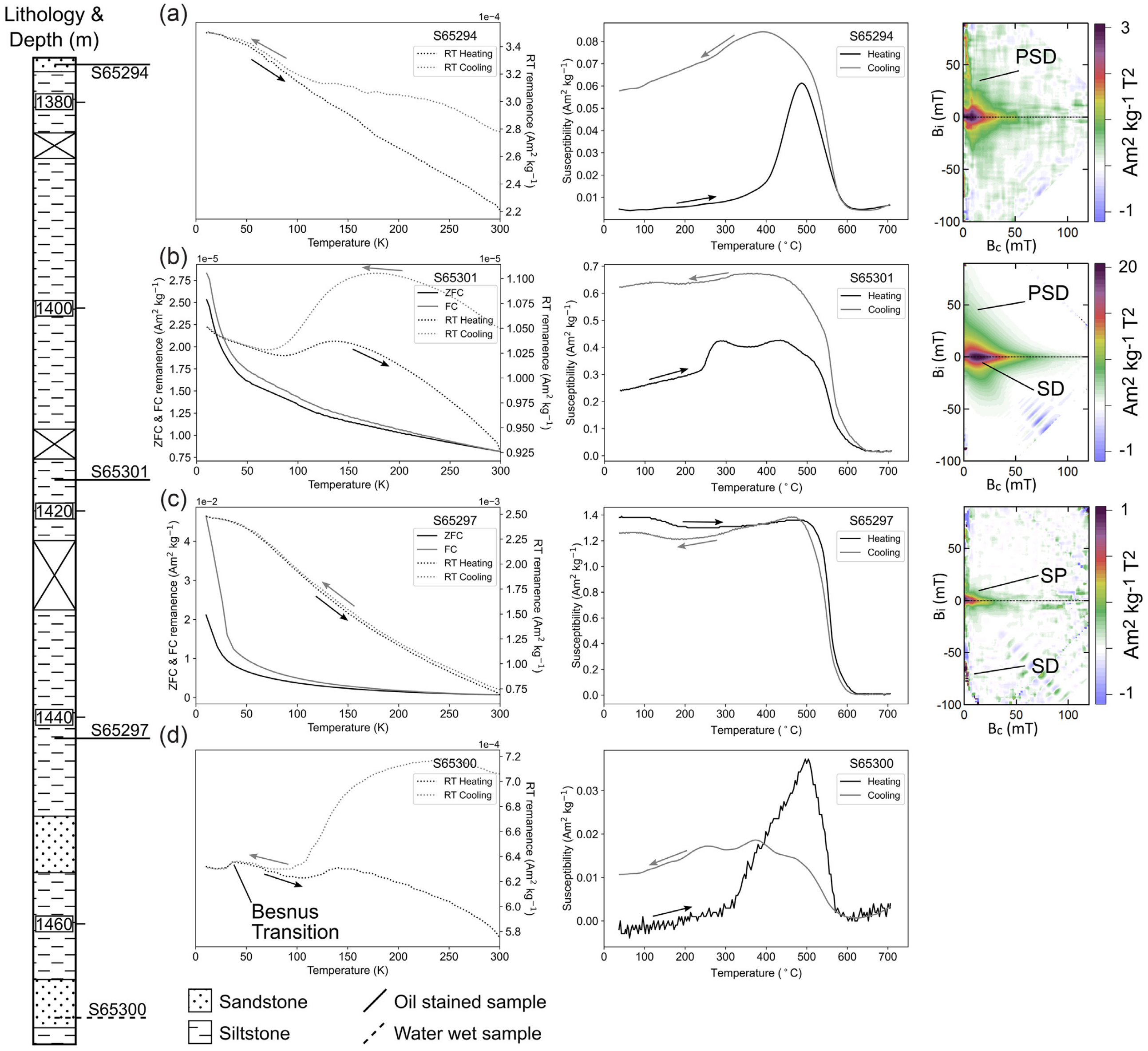

Figure 4. Representative samples from well 21/28a-03 (oil) showing the magnetic data (low-temperature magnetometry, high-temperature susceptibility (heated in Ar) and FORC diagrams) for four samples: (a) s65294, (b) s65301, (c) s65287 and (d) s65300 (no FORC diagram). S65294 consists of iron sulphides, some siderite and magnetite, with FORC data that indicates PSD gains. s65301 consists of maghemite and iron sulphides, and the FORC diagram in indicative of PSD or multiaxial-anisotropy SD grains. S65287 contains siderite, magnetite and iron sulphides, and the FORC diagram suggests the presence of SP and SD grains. s65300 consists of maghemite and iron sulphides. VARIFORC parameters (Egli 2013) for smoothing FORCs are sc,0 = 2, sc,1 = 4, sb,0 = 3, sb,1 = 4 and λcd = λb = 0.1, measuring time = 200 ms.

and in the dry well samples (Fig. 6), suggesting that monoclinic pyrrhotite is not associated with oil-staining but rather a background signal.

4.1.3 High-temperature susceptibility measurements

A total of 177 high-temperature susceptibility curves were used to aid identification of magnetic mineralogies (Figs 3–6); the remaining samples were magnetically too weak to measure. Due to chemical alteration during laboratory heating (Ar does not fully suppress this), determining the initial magnetic minerals can be complicated. When heating samples with a high concentration of siderite, for example s72392 and s63654 (Fig. 3), the initial susceptibility is generally relatively low on heating from room temperature to about 400 °C where the susceptibility increases (Housen *et al.* 1996). A sharp drop is typically noticed around ∼570 °C, suggesting alteration of siderite to magnetite. On cooling from 700 °C the susceptibility rapidly increases between 570 and 545 °C to values much higher than the heating susceptibility curve (> 50 per cent higher) indicating the continued formation of magnetite. A Hopkinson-like peak below the Curie temperature on cooling is typically observed, for example s63656 in Fig. 3(d). In many cases the presence of siderite was confirmed by low-temperature measurements, for example s72392 and s63654 (Fig. 3), Siderite was also identified in the dry-core samples, for example s70404 (Fig. 6c).

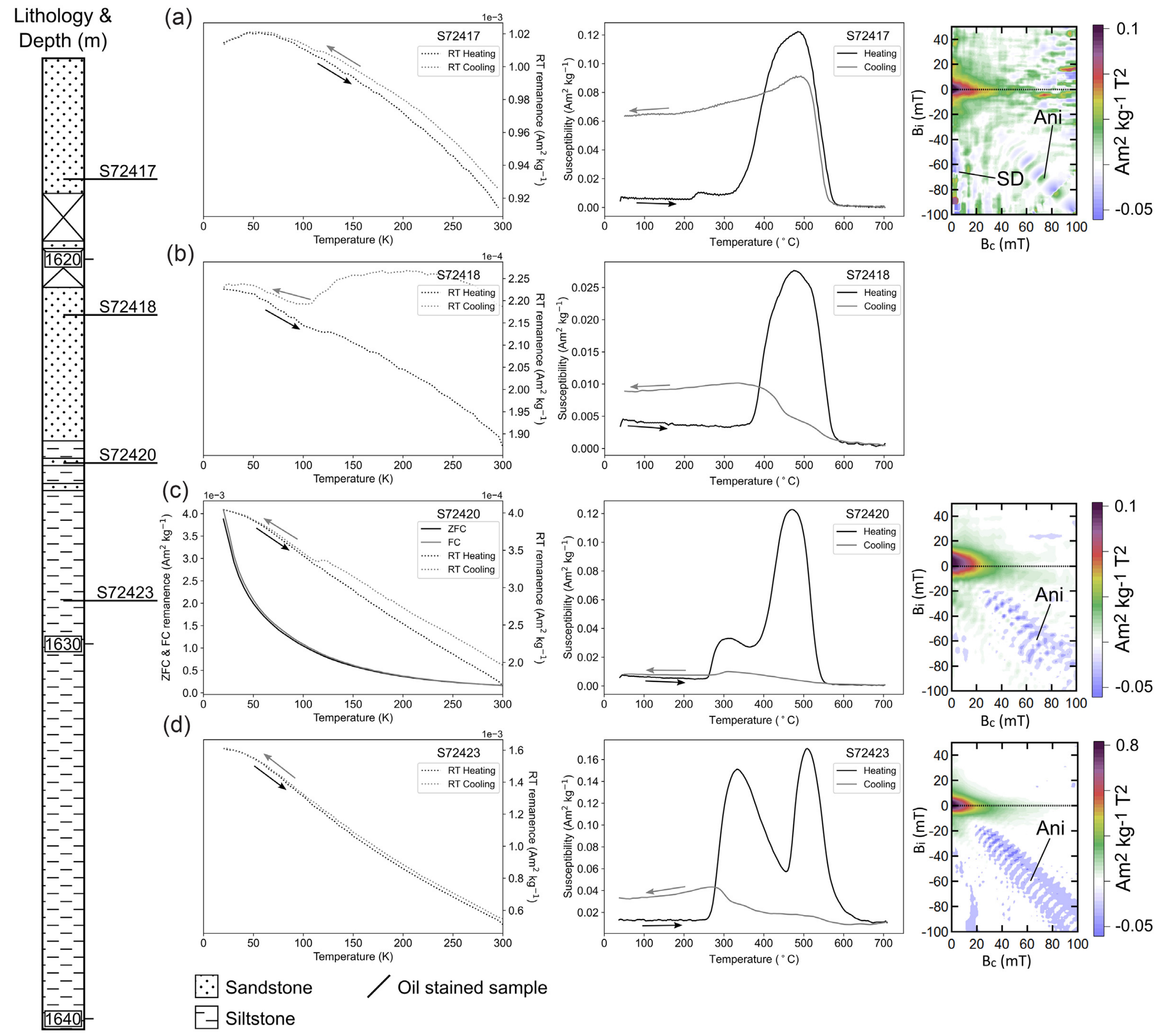

Figure 5. Representative samples from well 21/24-03 (oil) showing the magnetic data (low-temperature magnetometry, high-temperature susceptibility (heated in Ar) and FORC diagrams) for four samples: (a) s72417, (b) s72418 (no FORC diagram), (c) s72420 and (d) s72423. Generally, there is an abundance of iron sulphides relative to siderite. s72417 contains iron sulphides and magnetite, whilst s72418 contains maghemite and iron sulphides. s72420 consists of iron sulphides and magnetite, whilst the FORC diagram indicates the particles are all SD, that is <100 nm. Sample s72423 contains iron sulphides in the SD and PSD domain states. 'Ani' marks the features, which are due to multiaxial anisotropy (Harrison & Lascu 2014; Valdez-Grijalva & Muxworthy 2019). VARIFORC parameters (Egli 2013) for smoothing FORCs are sc,0 = 2, sc,1 = 4, sb,0 = 3, sb,1 = 4 and λcd = λb = 0.1, measuring time = 200 ms.

The high-temperature measurements showed clear evidence for iron sulphides; iron sulphides typically decompose on heating between 200 and 400 °C (Bol'shakov & Dolotov 2011). The low-temperature measurements found little evidence for monoclinic pyrrhotite, and the absence of lambda transitions in any of the high-temperature susceptibility experiments suggests no hexagonal pyrrhotite was present (Schwarz & Vaughan 1972). We therefore interpret the iron sulphide signal as being a mixture of pyrite and greigite; where greigite is present, authigenic pyrite is usually also present (Roberts 2015). We particularly tried to identify greigite: samples thought to contain greigite typically portray different high-temperature susceptibility heating and cooling behaviours. The reported greigite behaviours are: (1) a noticeable drop in susceptibility on heating in the range 350–450 °C, for example s63651, s65310 and s72423 (Figs 3a, 4b and 5d) (Bol'shakov & Dolotov 2011), (b) kinks in susceptibility on heating accompanied by a noticeable increase in susceptibility 250–450 °C, for example s72417 (Fig. 5a) (Dekkers *et al.* 2000), and (3) an increase in susceptibility on heating between 350 and 450 °C accompanied by a lower susceptibility on cooling, which noticeably increases on cooling below 500 °C, for example s65300 and s72418 (Figs 4d and 5b). However, it is still difficult to differentiate between the pyrite and greigite in the presence of other ferromagnetic minerals, for example magnetite, therefore we refer to the pyrite and greigite combined signal as the iron sulphide signal; this term does not include pyrrhotite.

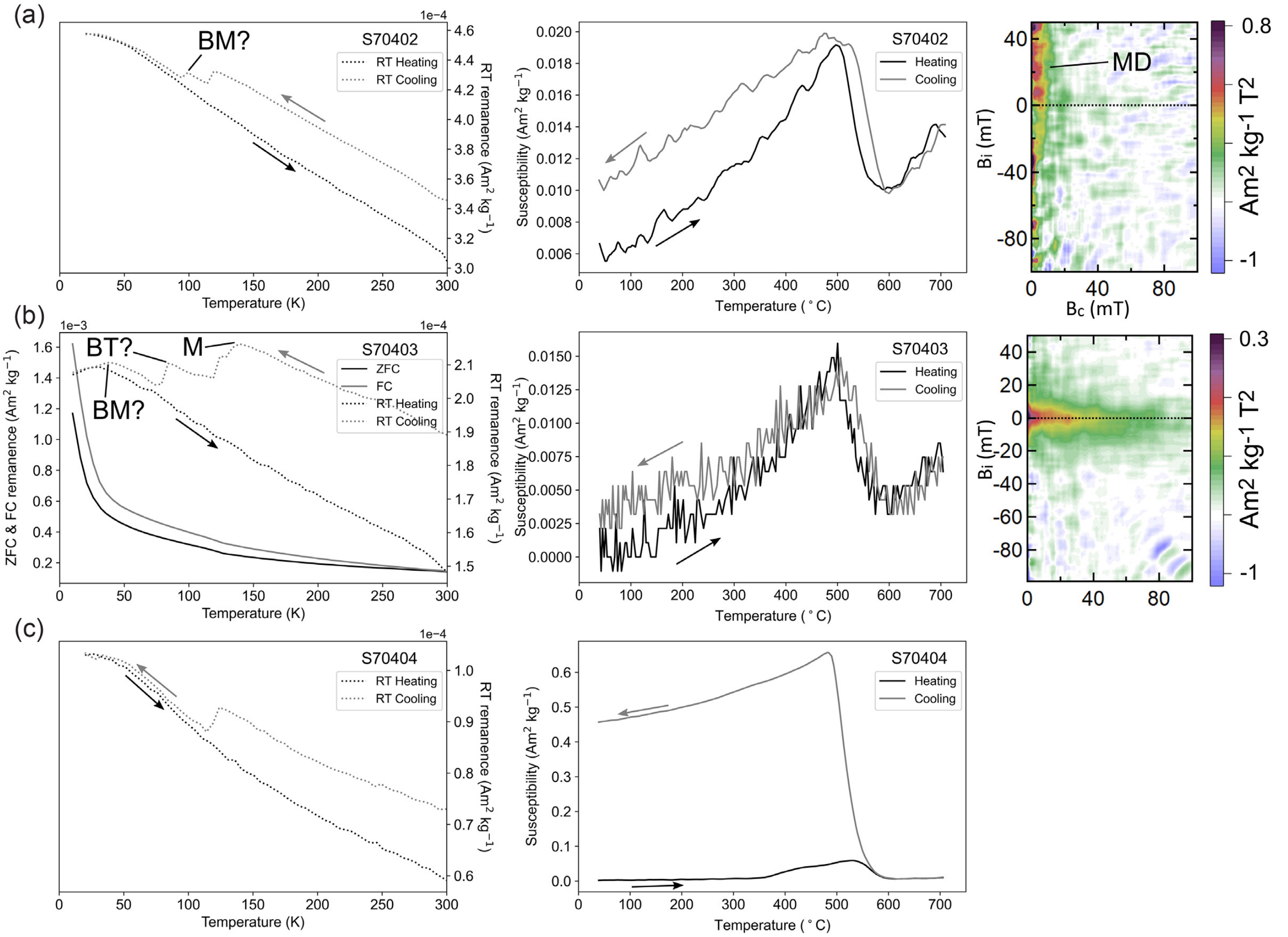

Figure 6. Magnetic data (low-temperature magnetometry, high-temperature susceptibility (heated in Ar) and FORC diagrams) for samples from dry 21/28b-07: (a) s70402, (b) s70403 and (c) s70404 (no FORC data). S70402 contains magnetite, and the FORC diagram indicates MD, that is >1000 nm. The s70403 experiments suggest the presence of magnetite and possibly monoclinic pyrrhotite and biogenic magnetite. The FORC diagram suggests the presence of a high-coercivity phase, that is either biogenic magnetite or pyrrhotite and (c) s70404 contains of magnetite and siderite. VARIFORC parameters (Egli 2013) for smoothing FORCs are sc,0 = 3, sc,1 = 3, sb,0 = 4, sb,1 = 3 and λc = λb = 0.1, measuring time = 200 ms. HT susceptibility measurements were heated in argon. BT, Besnus transition; BM, biogenic magnetite and M, magnetite.

4.2 Scanning electron microscopy

To help distinguish between pyrrhotite and greigite, which can be challenging magnetically when only fields <1 T are available during hysteresis, and to help characterize the samples in general, SEM imaging was carried out on extracted and non-extracted samples suspected to contain iron sulphides (Fig. 7). EDX analysis of the crystals in Figs 7(a)–(c), identified iron and sulphur; although the EDX was not calibrated to identify between greigite and pyrite, the recorded ratios of iron and sulphur suggest that these crystals were likely to be greigite or pyrite as marked in the figure; greigite is typically cubic and pyrite crystals can either be cubic or euhedral (Roberts 2015). In Fig. 7(a) the greigite or pyrite grains were 40–170 nm in size (Fig. 7a). The two fused framboids in Fig 7(b) consist of euhedral particles 500 nm to 1.5 µm sized grains, which are likely pyrite. We suggest that these framboids are likely formed after the pyritization of greigite framboids (Wilkin & Barnes 1997) (Fig. 7b). In Fig. 7b, the framboids also appear to be flanked by smaller (<100 nm) iron sulphide grains (Fig. 7b). The elongated framboid shown in Fig. 7(c) is made up of 30–100 nm sized particles, which are likely to be greigite. The SEM imaging also shows evidence for microbial activity in s65311 and s65328 (Figs 7d and e). No crystal structure akin to monoclinic or hexagonal pyrrhotite was observed in the SEM images; monoclinic pyrrhotite appears needle like, and hexagonal pyrrhotite crystals have a hexagonal structure (Roberts 2015). This does not rule out their presence as the SEM images only represent a small sample volume.

4.3 Geochemical analysis

Extracted aliphatic fractions from water-wet samples s70402, s70403 and s70404 from dry wells, were analysed in the GC-MS for compound identification. The flat response of the aliphatic mass chromatograph (raw data available in Badejo 2019) and the lack of biomarker suggest there is no evidence of oil in the samples (Peters *et al.* 2006). The GC-MS sensitivity was ∼1 ppm. Oil-stained sandstones from reservoirs charged by type II source rocks in the UK can have aliphatic contents ranging from 39 to 48 per cent (Barnard & Bastow 1991; Emmerton *et al.* 2013b; Abubakar *et al.* 2020). These results suggest the rock magnetic experiments carried out on the dry core sample likely represent a true background sample.

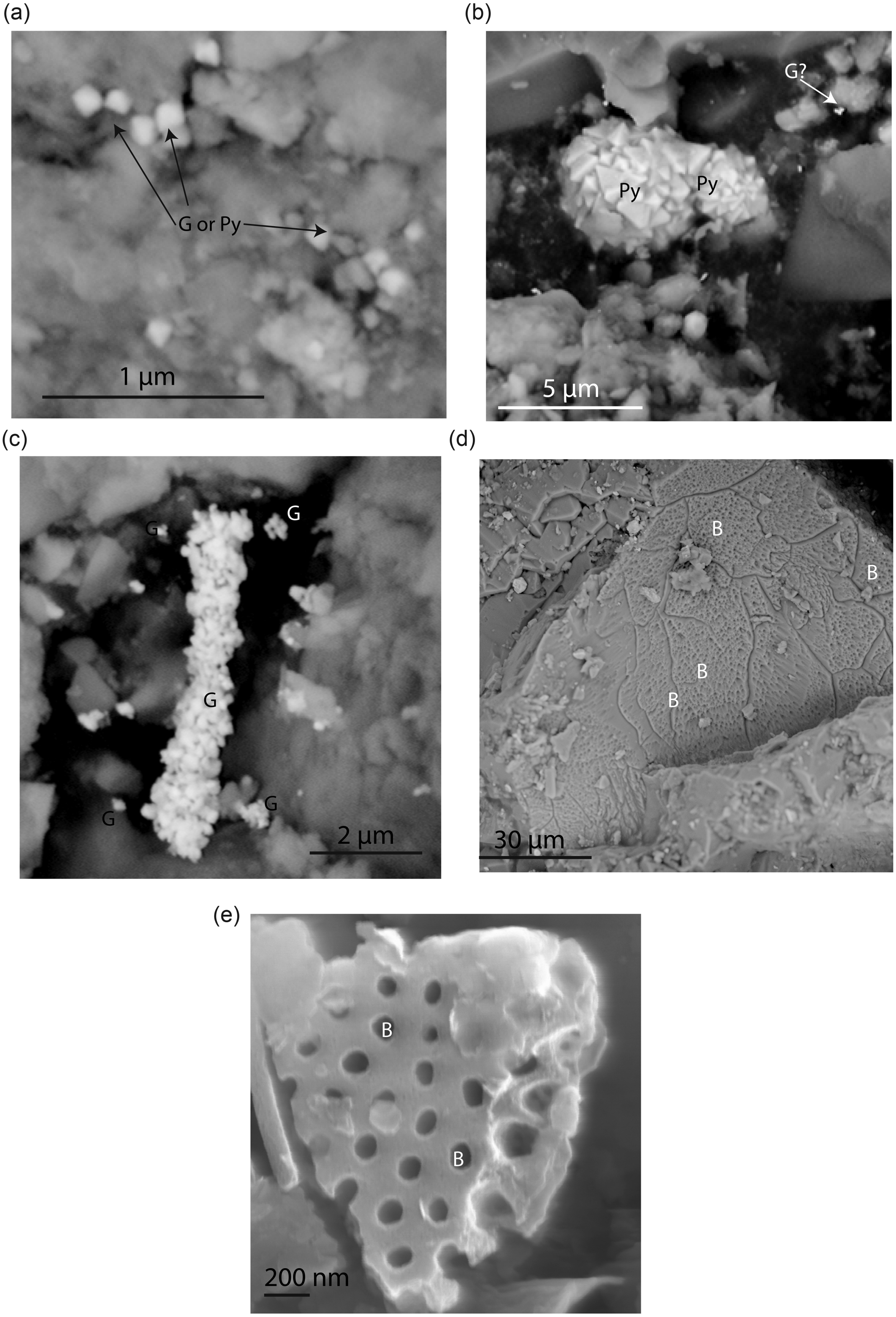

Figure 7. SEM Images showing: (a) crystals identified as greigite (G) or pyrite (Py) in s65329, (b) two fused coarse-grained euhedral pyrite framboids surrounded by possibly smaller cubic greigite crystals in s65328, (c) an elongated framboid—likely to be greigite—in s65311, (d) evidence of bioturbation in s63594 highlighted with a 'B', and (e) evidence for bioturbation in s65328, also highlighted with a 'B'. Images a-c are backscattered electron images obtained with a Phenom SEM while images d–e are backscattered electron images obtained with a Leo SEM.

5 DISCUSSION

Rock magnetic experiments identified a range of magnetic minerals present in the samples including magnetite, maghemite, titanohematite, goethite, siderite and the iron sulphides pyrite, monoclinic pyrrhotite and likely greigite; however, the magnetic minerals magnetite, siderite and the iron sulphides (likely greigite and pyrite) dominated the magnetic signature in the oil samples (Figs 3–5, Table 1). Magnetite was the dominant mineral in the dry-well samples (Fig. 6, Table 1). There was evidence for an abundance nanometric magnetic minerals, that is $<$50nm in size. Typical concentrations for the ferromagnetic (*sensu lato)* minerals was ∼10–200 pm, and ∼2000–20 000 ppm for the paramagnetic minerals (Table 2). There was no geochemical evidence for oil in the dry-well samples.

5.1 Origin of the magnetic signals

Based on our data, we group the magnetic minerals observed into background or source signal in Table 2. Source signal minerals relates to minerals precipitated due to the presence of hydrocarbons, while the background signal relates to minerals that are independent of the presence of hydrocarbons. Although traces of titanohematite and goethite were found in oil-well samples (Figs 3–5), they were more dominant in the background magnetic signal (Fig. 6). Titanohematite is most likely detrital and derived from the mechanical weathering of parent rock. The origin of goethite is harder to identify. It could be detrital, derived from the weathering of primary iron-bearing minerals, or as is more likely it is ‘authigenic’, but has formed post-coring. The core samples have been stored in air for more than two decades, and oxidation of the iron sulphides present in the samples is known to lead to the formation of goethite (Rochette & Fillion 1989).

Magnetite was present in almost all the oil well and dry well core samples (Figs 3–6). The occurrence of magnetite in the dry-well core samples suggest it is detrital, but it could also be authigenic as studies have shown it to be precipitated in the reducing conditions generated by hydrocarbons (Machel & Burton 1991); in the presence of refined oil where sulphur has been removed, magnetite has been shown to form in contaminated soil (Rijal *et al.* 2010; Ameen N.N. *et al.* 2014). FORC diagrams from the dry wells suggests that the detrital magnetite consists of larger MD grains ($>$1000 nm), for example s70402 (Fig. 6). There was no evidence for such large MD magnetite grains in the oil-stained samples (Figs 3–5), and the observed magnetite was smaller, likely $<$100 nm, suggesting that it was authigenic in agreement with previous studies (Elmore *et al.* 1993; Abubakar *et al.* 2020). Maghemite seen in samples s72392 and s65300 (Figs 3b and 4d), is most likely a product of the oxidation of magnetite (Özdemir & Dunlop 2010), probably in the core store.

Siderite was observed in many of the samples. Siderite is typically of authigenic origin in sedimentary settings and is often found as a diagenetic cementing agent; it was observed in both the oil- and dry-well cores (Figs 3–6). Diagenetic changes in temperature, an increase in total inorganic carbon or a bacterial reduction of Fe^{2+} can lead to the precipitation of siderite in the dry wells (Ellwood *et al.* 1988; Machel & Burton 1991). The reducing environment created by hydrocarbon also promotes the replacement of hematite and magnetite by siderite in the oil wells (Burton *et al.* 1993).

Iron sulphides were only identified in the oil wells, for example samples s63651, s65310 and s72423 (Figs 3a, 4b and 5d), suggesting that hydrocarbons induced the precipitation of iron sulphide. We found no evidence for pyrrhotite, but did for pyrite and possibly greigite, however, given that magnetite was identified in all the samples it is difficult to quantify the relative abundance of pyrite and greigite in the sample (Fig. 7). The growth mechanisms for greigite and pyrite are similar, therefore we treat them as a single iron sulphide signal. There are several possible mechanisms for this greigite and pyrite formation: (1) Abubakar *et al.* (2015) demonstrated that source rocks in the oil kitchen can precipitate nanometric greigite ($<$100 nm), (2) diagenetic changes caused by hydrocarbon presence, are known to lead to the replacement of magnetite, hematite or siderite by iron sulphides such as greigite and pyrite (Burton *et al.* 1993; Emmerton *et al.* 2012) and (3) anaerobic biodegradation by sulphate reducing bacteria generates reduced sulphur (HS^- and H_2S) which reacts with dissolved Fe^{2+} (from replacement or dissolution of magnetite or hematite) to form diagenetic greigite (Reynolds *et al.* 1990).

5.2 Variation of magnetic minerals along the fill-spill chain

We made estimates of the concentrations of the magnetic minerals present in Table 2. The variation in magnetic properties between the samples with the same basic mineralogy (Table 1) is greater than between wells of differing mineralogies. It is therefore the identification of the magnetic minerals present, which is key to understanding the effect of hydrocarbons on the magnetic signature. These observations have led us to classify the samples into five types of magnetic mineralogies described below:

(1) Siderite-rich samples: This class consists of samples were the low- and high-temperature experiments confirm the presence of siderite, but there is no evidence for iron sulphides, for example s63654 and s63656 (Figs 3c, d).

(2) Siderite-rich samples with some iron sulphides: This class consist of samples where the low-temperature experiments confirm the presence of siderite and the high-temperature susceptibility data suggest the presence of iron sulphides (likely greigite and pyrite). The susceptibility data on cooling display Hopkinson peaks at ∼570 °C with the cooling susceptibility curve much higher than the susceptibility on heating ($>$100 per cent increase in susceptibility), for example s63651 (Fig. 3a).

(3) Iron-sulphide-rich samples with some siderite: This class consists of samples where the high-temperature susceptibility on heating suggests the presence of iron sulphides, that is likely greigite and pyrite. The susceptibility cooling curve is usually as high or higher than the heating curve, which hints at the presence of some siderite in the sample, for example s65297 (Fig. 4c).

(4) Iron-sulphide-rich samples: This class consists of samples with high-temperature susceptibility on heating and cooling behaviour like s72418, s72420 and s72423 (Figs 5b–d). We interpret this as being a greigite and pyrite signal.

(5) Magnetite-rich sample: This class consists of samples with a nearly reversible high-temperature susceptibility curve, for example s70402 and s70403 (Fig. 6).

To aid spatial visualization of the data, each sample is placed in one of the five classes above, and the dominant mineral assemblage for a given well assigned to the majority sample class (Fig. 8). There are clear variations in the relative abundance of siderite and iron sulphides (likely pyrite and greigite) along the migration pathway in the core samples; siderite dominates the signal in the east and becomes less prominent as the presence of iron sulphides increases in the west.

Table 2. Origin of the magnetic minerals found in this study. Groups of magnetic minerals belong to background and source signals, that is directly related to the presence of hydrocarbon. Background signals are minerals that are likely present prior to the invasion of oil, while the source signal refers to minerals precipitated or introduced after the charging of the well by oil. Goethite and maghemite are thought to form via storage in air in the core store (>30 yr). Estimations of typical concentrations are provided; these are thought to be typical values, with large variations between the samples. In cases where the presence is very low and unquantifiable 'identifiable' has been given.

Magnetic mineral	Detrital	Authigenic	Typical concentrations (ppm)	Background or source signal
Titanohematite	✓		identifiable	Background
Pyrrhotite	✓		identifiable	Background
Goethite	✓	✓	identifiable	Background; likely post-coring
Magnetite	✓	✓	10–100	Background and source
Maghemite		✓	identifiable	Oxidation product of magnetite; likely post-coring
Siderite		✓	2000–7000	Background and source
Greigite		✓	10–200	Source
Pyrite		✓	5000–20 000	Source

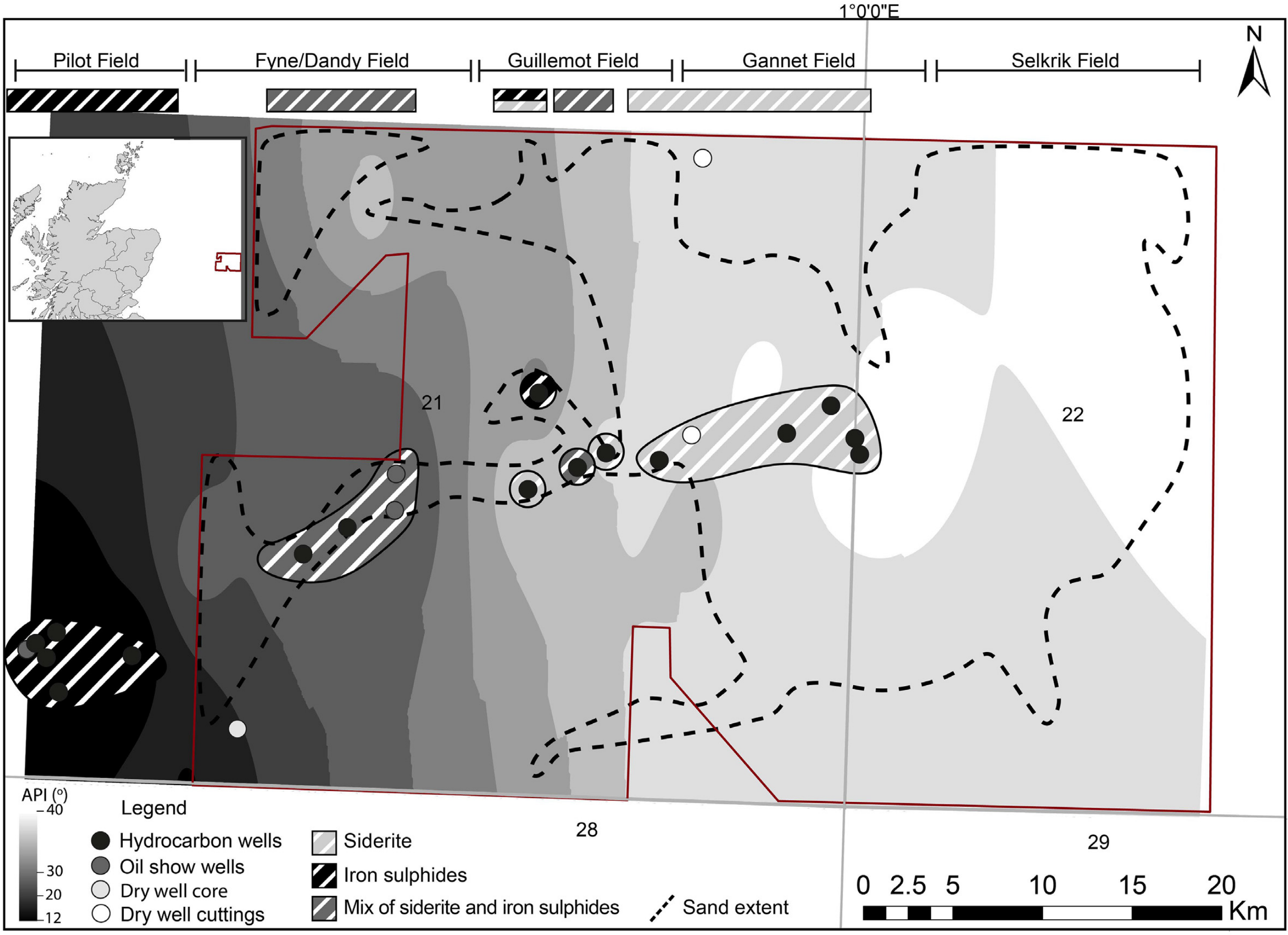

Figure 8. Distribution of siderite and iron sulphides (likely pyrite and greigite) in the core samples from the Tay fan. The abundance of iron sulphides increases along the lateral migration pathway from west to east. An interpolation of API gravity is also plotted, increasing from east to west. The red line denotes the Tay fan, the black is the 3-D data coverage and red circles are the locations of the wells used to generate the contour plot. API data was obtained from purchased geochemical reports from HIS Markit. Some well names are included for referencing. Insert shows the location of the map.

5.3 Using the mineral magnetic signal to aid petroleum system modelling

3-D petroleum systems modelling of migration into the TSM (Badejo *et al.* 2021a), suggests vertical hydrocarbon migration is prominent in the east (Gannet Field), while a mixture of vertical and lateral migration in the centre (Guillemot Field) and lateral migration prominent in the west (Fyne/Dandy to Pilot Field) (Fig. 1).

The rock magnetic results suggest a dominant siderite signal in the east, which decreases westward, becoming increasingly dominated by iron sulphides (Fig. 8). Comparing this with the magnetic data, we suggest that the siderite signal can be attributed to vertical migration, while the iron sulphide signal can be attributed to lateral migration (Fig. 9). This observation helped in constraining 3-D models (Badejo *et al.* 2021a); the initial 3-D model developed without the magnetic mineralogy input, had no accumulation of oil

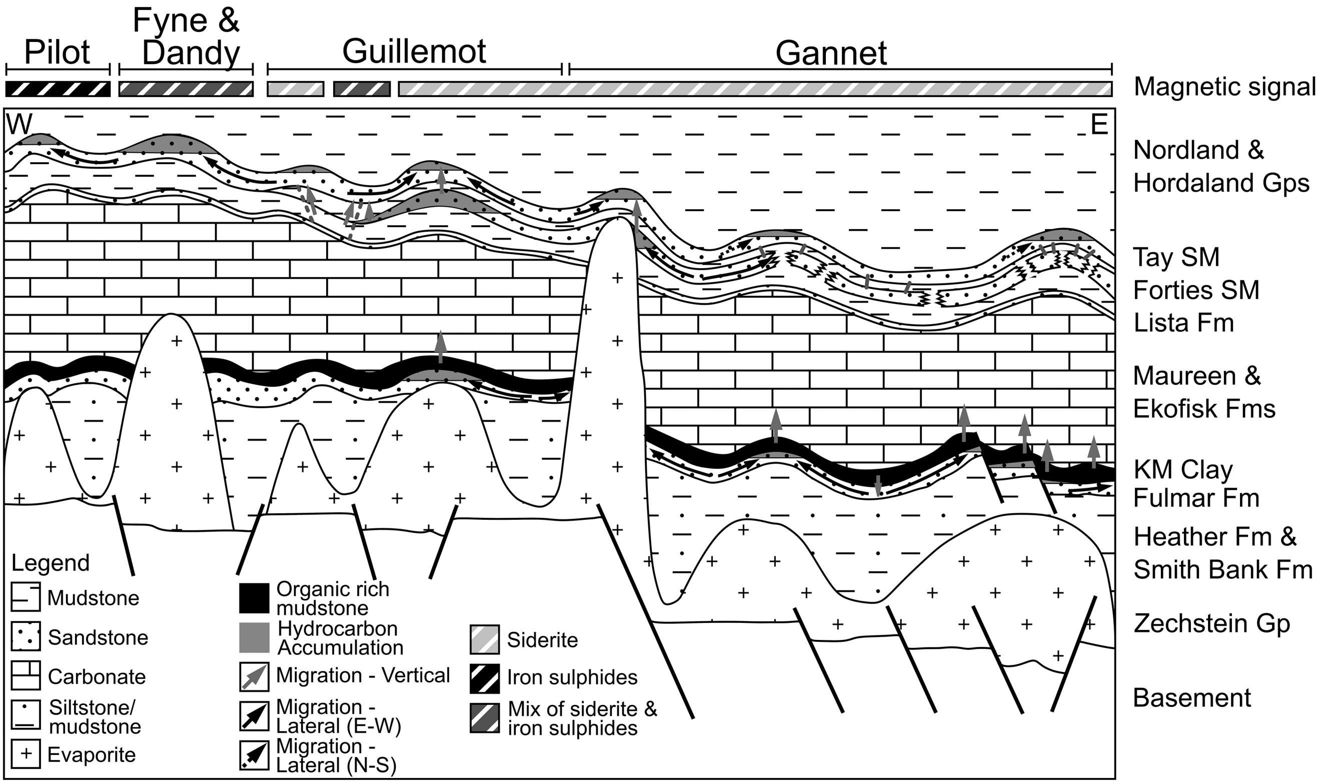

Figure 9. Schematic of the magnetic results plotted on a 2-D slice of the 3-D model made by Badejo (2019) and Badejo *et al.* (2021a). The schematic shows the siderite-rich signal in areas dominated with vertical migration and an increasing presence of iron sulphides (likely greigite and sulphide) along the lateral migration pathway. Diagram is not drawn to scale.

in the wells located in the west (Badejo 2019). We noticed that well 21/29a-08 in the west has a dominant siderite signal unlike the surrounding wells that have a mixture of siderite and iron sulphides (Fig. 8) suggesting that this structure could have been charged vertically similarly to the structures in the east. The 3-D seismic data was reassessed, and on closer inspection large scale injectites were observed in the west and included in the basin model (Badejo *et al.* 2021a). This led to the construction of successful petroleum systems model with charging of the structures in the west (Fig. 9).

There is one structure that does not fit this simple model, that is siderite is associated with vertical migration and iron sulphide with lateral migration, that is well 21/24-03. The 3-D model suggested well 21/24-03 was charged both laterally and vertically in its history (Badejo *et al.* 2021a), but it is dominated by an iron sulphide signal (Fig. 8). This suggests the correlation of a siderite or an iron sulphide dominant signal to vertical or lateral migration pathways might be coincidental. We propose a biodegradation mechanism to account for this observed variation.

5.3.1 Biodegradation model

Progressive biodegradation of oil by microbes at temperatures <80 °C results in the removal of saturated hydrocarbons and an increase in the heavy asphaltene and polar oil constituents (Wenger *et al.* 2002). This decreases the oil quality by increasing the viscosity, sulphur and metal content while reducing its API (American Petroleum Institute) gravity (Head *et al.* 2003). The sulphur combines with hydrogen giving rise to high concentrations of hydrogen sulphide (H_2S), that combines with available iron precipitating nanoparticles of iron sulphide in the reservoir (Mann *et al.* 1990); thermostability phase diagrams suggests iron sulphides are stable in high concentrations of sulphur, while iron oxides reduce to iron sulphide phases (Burton *et al.* 1993). These phase diagrams also predict the alteration of magnetite to siderite in relatively lower concentrations of sulphur, while hematite alters to pyrite (Burton *et al.* 1993).

Volkman *et al.* (1983) have correlated API gravity to levels of biodegradation using a database of North Sea oils. The results suggested APIs >30° implies the oil is not degraded. APIs between 30° and 22° suggests moderate biodegradation, while APIs <22° suggest extensive biodegradation which is considered extreme at values <15° (Barnard & Bastow 1991).

Geochemical data from 25 wells was used to generate a contour plot showing the variation of API gravity in the Tay fan (Fig. 8), where it is clearly seen that the APIs decrease from 40° to 35° in the east to <16° in the west (Pilot). Emmerton *et al.* (2013b) linked the presence of MD hematite and magnetite to biodegradation, but this study suggests that the degree of biodegradation (Fig. 8) is proportional to the presence of iron sulphide (Figs 3–6 and 8).

The oil in well 21/24-03 has an API of 27° (Fig. 8), but has an iron sulphide dominated signal as opposed to a mixture of siderite and iron sulphide seen in other samples with moderate biodegradation (Fig. 8). The filling history of this structure (Fig. 9) may explain the observed differences (Badejo *et al.* 2021a): The structure of well 21/24-03 was charged at ∼8 Ma when the temperature was <55 °C, low enough for biodegradation and iron sulphide formation, which would have continued until ∼5 Ma when it was charged with fresh oil followed by rapid burial, which caused a temperature increase. This fresh charging and reduction in biodegradation would have increased the oil quality and the API (Head *et al.* 2003); however, there was still sufficient sulphur present to allow iron sulphide to remain stable (Kao *et al.* 2004). This suggests the presence of iron sulphide could be an indicator of paleo-biodegradation of oil in the reservoir. This may explain why iron sulphide is present in some high API oil wells, for example 21/29a-06 (Fig. 8).

6 CONCLUSIONS

Rock magnetic measurements were carried out to determine the mineralogy and grain-size of the magnetic minerals present in samples from oil and dry wells in the Tay fan of the Central North Sea. The following observations were made:

(1) High- and low-temperature magnetic experiments identified the presence of magnetite, maghemite, titanohematite, goethite, siderite, pyrite and likely greigite in the samples from oil wells (Figs 3–5), while magnetite, biogenic magnetite, titanohematite, goethite, siderite and possibly monoclinic pyrrhotite were observed in samples from the dry well (Fig. 6).

(2) Titanohematite and goethite were classed as background signals while iron sulphide was classed as a hydrocarbon signal. Magnetite and siderite could be either a background or hydrocarbon signal (Table 2).

(3) FORC diagrams suggested the presence of SP, SD and PSD grains in the oil well samples (Figs 3–5), that is <1000 nm assuming greigite or magnetite, while the dry well contain mostly and MD signals (Fig. 6), i.e., >1000nm assuming greigite or magnetite.

(4) Magnetite was present in most samples, but relative variations in the abundance of siderite and iron sulphide was observed and linked to hydrocarbon migration (Figs 8 and 9))

(5) Synthesising the results showed the dominance of siderite in the east and the dominance of iron sulphide in the west with a zone of mixing in the middle (Fig. 8).

(6) Typical concentrations for the ferromagnetic (*sensu lato)* minerals was ∼10–200 pm, and ∼2000–20 000 ppm for the paramagnetic minerals (Table 2).

The organic biodegradation mechanism proposes the variation observed in Fig. 8 is caused by an increase in the severity of biodegradation along the migration pathway leading to the precipitation of more iron sulphides in the west (Fig. 9). The change to a dominant siderite signal in the west (21/29a-08 in Fig. 8) suggests fresh hydrocarbon charge from below preventing severe biodegradation and retarding the precipitation of iron sulphide. This observation led to the identifications of injectites and the construction of a 3-D petroleum system model (Badejo *et al.* 2021a)). It is recommended that mineral magnetic methods can be used to constrain 3-D petroleum system models of mature hydrocarbon reservoir systems, thereby increasing yield from existing reservoir systems and reducing the need for future exploitation of untapped hydrocarbon reservoirs.

ACKNOWLEDGEMENTS

SAB acknowledges funding from the Petroleum Technology Development Fund (PTDF) Nigeria, and two Visiting Fellowships to the Institute of Rock Magnetism (IRM), University of Minnesota. The IRM is funded by the National Science Foundation, and by the University of Minnesota. Schlumberger is thanked for the Petrel and PetroMod software used in this study.

DATA AVAILABILITY

All the data as part of this study including the wire-line log data are available in the appendix of the PhD thesis of Badejo (2019) available from www.spiral.imperial.ac.uk.

REFERENCES

Abubakar, R., Muxworthy, A.R., Fraser, A., Sephton, M.A., Watson, J.S., Heslop, D., Paterson, G.A. & Southern, P., 2020. Mapping hydrocarbon charge-points in the Wessex Basin using seismic, geochemistry and mineral magnetics, *Mar. Pet. Geol.,* **111,** 510–528.

Abubakar, R., Muxworthy, A.R., Sephton, M.A., Southern, P., Watson, J.S., Fraser, A.J. & Almeida, T.P., 2015. Formation of magnetic minerals in hydrocarbon-generation conditions, *Mar. Pet. Geol.,* **68,** 509–519.

Aldana, M., Costanzo-Alvarez, V., Gomez, L., Gonzalez, C., Diaz, M., Silva, P. & Rada, M., 2011. Identification of magnetic minerals related to hydrocarbon authigenesis in Venezuelan oil fields using an alternative decomposition of isothermal remanence curves, *Stud. Geophys. Geod.,* **55,** 343–358.

Ameen, N.N., Klueglein, N., Appel, E., Petrovsky´, E., Kappler, A. & Leven, C., 2014. Effect of hydrocarbon-contaminated fluctuating groundwater on magnetic properties of shallow sediments, *Stud. Geophys. Geod.,* **58,** 442–460.

Badejo, S.A., 2019. Using magnetic techniques to calibrate lateral hydrocarbon migration in basin modelling: a case study from the lower tertiary, *PhD thesis*, Imperial College London, UK Central North Sea,

Badejo, S.A., Fraser, A.J., Neumaier, M. & Muxworthy, A.R., 2021a. 3D Petroleum Systems Modelling as an exploration tool in mature basins: a case study from the Central North Sea, UK, *Mar. Pet. Geol.,* submitted.

Badejo, S.A., Muxworthy, A.R. & Fraser, A.J., 2021b. Magnetic enhancement at the oil-water and gas-oil contacts in hydrocarbon systems, *AAPG Bull.,*.

Banner, J., Chatellier, J., Feurer, J. & Neuhaus, D., 1992. Guillemot D: a successful appraisal through alternative interpretation, *Geol. Soc., Lond., Spec. Publ.,* **67,** 129–149.

Barnard, P.C. & Bastow, M.A., 1991. Hydrocarbon generation, migration, alteration, entrapment and mixing in the Central and Northern North Sea, *Geol. Soc., Lond., Spec. Publ.,* **59,** 167–190.

Besnus, M. & Meyer, A., 1964. Nouvelles données expérimentales sur le magnétisme de la pyrrhotine naturelle, in *Proc. Int. Conf. Mag,* pp. 507–511, Nottingham.

Bol'shakov, V.A. & Dolotov, A.V., 2011. The Curie temperature of the natural greigite: a new interpretation of the thermomagnetic data, *Doklady Earth Sci.,* **440,** 1431–1434.

Burton, E.A., Machel, H.G. & Qi, J., 1993. Thermodynamic constraints on anomalous magnetization in shallow and deep hydrocarbon seepage environments, in *Applications of Paleomagnetism to Sedimentary Geology*pp. 193–207, eds Aïssaoui, D.M., McNeill, D.F. & Hurley, N.F., SEPM Society for Sedimentary Geology.

Carvallo, C., Muxworthy, A.R., Dunlop, D.J. & Williams, W., 2003. Micromagnetic modeling of first-order reversal curve (FORC) diagrams for single-domain and pseudo-single-domain magnetite, *Earth Planet. Sci Lett.,* **213,** 375–390.

Cayley, G., 1987. *Hydrocarbon Migration in the Central North Sea: Proceedings of the 3rd Conference on Petroleum Geology of North West Europe Held at the Barbican Centre, London, 26-29 October 1986,* Vol. **2,** Graham and Trotman, pp. 549–555.

Chang, L., Roberts, A.P., Williams, W., Fitz Gerald, J.D., Larrasoaña, J.C., Jovane, L. & Muxworthy, A.R., 2012. Giant magnetofossils and hyperthermal events, *Earth Planet. Sci Lett.,* **351–352,** 258–269.

Costanzo-Alvarez, V., Aldana, M., Aristeguieta, O., Marcano, M.C. & Aconcha, E., 2000. Study of magnetic contrasts in the Guafita oil field (South-Western Venezuela), *Phys. Chem. Earth,* **25,** 437–445.

Dekkers, M.J., Passier, H.F. & Schoonen, M.A.A., 2000. Magnetic properties of hydrothermally synthesized greigite (Fe3S4)—II. High- and low-temperature characteristics, *Geophys. J. Int.,* **141,** 809–819.

Donovan, T.J., Hendricks, J.D., Roberts, A.A. & Eliason, P.T., 1984. Low-altitude aeromagnetic reconnaissance for petroleum in the Arctic National Wildlife Refuge, Alaska, *Geophysics,* **49,** 1338–1353.

Egli, R., 2013. VARIFORC: an optimized protocol for calculating non-regular first-order reversal curve (FORC) diagrams, *Glob. Planet. Change,* **110,** 302–320.

Ellwood, B.B., Chrzanowski, T.H., Hrouda, F., Long, G.J. & Buhl, M.L., 1988. Siderite formation in anoxic deep-sea sediments: a synergetic bacteria controlled process with important implications in paleomagnetism, *Geology,* **16,** 980–982.

Elmore, R.D., Imbus, S., Engel, M.H. & Fruit, D., 1993. Hydrocarbons and magnetizations in magnetite, *SEPM Special Publication: Applications of Paleomagnetism to Sedimentary Geology,* Vol. **49,** pp. 181–191, eds Aïssaoui, D.M., McNeill, D.F. & Hurley, N.F., SEPM Society for Sedimentary Geology.

Emmerton, S., Muxworthy, A.R. & Sephton, M.A., 2012. Magnetic characterization of oil sands at Osmington Mills and Mupe Bay, Wessex Basin, UK, *Geol. Soc., Lond., Spec. Publ.,* **371,** 189–198.

Emmerton, S., Muxworthy, A.R. & Sephton, M.A., 2013a. A magnetic solution to the Mupe Bay mystery, *Mar. Pet. Geol.,* **46,** 165–172.

Emmerton, S., Muxworthy, A.R., Sephton, M.A., Aldana, M., Costanzo-Alvarez, V., Bayona, G. & Williams, W., 2013b. Correlating biodegradation to magnetization in oil bearing sedimentary rocks, *Geochim. Cosmochim. Acta,* **112,** 146–165.

Guyodo, Y., LaPara, T.M., Anschutz, A.J., Penn, R.L., Banerjee, S.K., Geiss, C.E. & Zanner, W., 2006. Rock magnetic, chemical and bacterial community analysis of a modern soil from Nebraska, *Earth planet. Sci Lett.,* **251,** 168–178.

Guzmán, O., Costanzo-Álvarez, V., Aldana, M. & Díaz, M., 2011. Study of magnetic contrasts applied to hydrocarbon exploration in the Maturín Sub-Basin (eastern Venezuela), *Stud. Geophys. Geod.,* **55,** 359–376.

Harrison, R.J. & Lascu, I., 2014. FORCulator: a micromagnetic tool for simulating first-order reversal curve diagrams, *Geochem. Geophys. Geosyst.,* **15,** 4671–4691.

Head, I.M., Jones, D.M. & Larter, S.R., 2003. Biological activity in the deep subsurface and the origin of heavy oil, *Nature,* **426,** 344.

Housen, B.A., Banerjee, S.K. & Moskowitz, B.M., 1996. Low-temperature magnetic properties of siderite and magnetite in marine sediments, *Geophys. Res. Lett.,* **23,** 2843–2846.

Isaksen, G.H., 2004. Central North Sea hydrocarbon systems: generation, migration, entrapment, and thermal degradation of oil and gas, *AAPG Bull.,* **88,** 1545–1572.

Jacobs, I.S., 1963. Metamagnetism of Siderite ($FeCO_3$), *J. Appl. Phys.,* **34,** 1106–1107.

Kao, S.-J., Horng, C.-S., Roberts, A.P. & Liu, K.-K., 2004. Carbon–sulfur–iron relationships in sedimentary rocks from southwestern Taiwan: influence of geochemical environment on greigite and pyrrhotite formation, *Chem. Geo.,* **203,** 153–168.

Liu, Q.S., Chan, L.S., Yang, T., Xia, X.H. & Cheng, T.J., 2006. Magnetic enhancement caused by hydrocarbon migration in the Mawangmiao Oil Field, Jianghan Basin, China, *J. Petrol. Sci. Eng.,* **53,** 25–33.

Machel, H.G. & Burton, E.A., 1991. Causes and spatial distribution of anomalous magnetization in hydrocarbon seepage environments, *AAPG Bull.,* **75,** 1864–1876.

Mann, S., Sparks, N.H.C., Frankel, R.B., Bazylinski, D.A. & Jannasch, H.W., 1990. Biomineralization of ferrimagnetic greigite (Fe_3S_4) and iron pyrite (FeS_2) in a magnetotactic bacterium, *Nature,* **343,** 258–261.

McCabe, C., Sassen, R. & Saffer, B., 1987. Occurrence of secondary magnetite within biodegraded oil, *Geology,* **15,** 7–10.

Nealson, P.H., 2009. Pore-throat sizes in sandstones, tight sandstones, and shales, *AAPG Bull.,* **93,** 329–340.

Özdemir, Ö. & Dunlop, D.J., 2010. Hallmarks of maghemitization in low-temperature remanence cycling of partially oxidized magnetite nanoparticles, *J. geophys. Res.,* **115,** doi:10.1029/2009JB006756.

Peters, K.E., Walters, C.C. & Moldowan, J.M.T., 2006. Biomarkers and isotopes in the environment and human history. in *The Biomarker Guide,* pp. 249–250, ed. Tyson, R.. Cambridge Univ. Press.

Reynolds, R.L., Fishman, N.S., Wanty, R.B. & Goldhaber, M.B., 1990. Iron sulfide minerals at Cement Oil Field, Oklahoma: implications for magnetic detection of oil fields, *Geol. Soc. Am. Bull.,* **102,** 368–380.

Rijal, M.L., Appel, E., Petrovský, E. & Blaha, U., 2010. Change of magnetic properties due to fluctuations of hydrocarbon contaminated groundwater in unconsolidated sediments, *Environ. Poll.,* **158,** 1756–1762.

Roberts, A.P., 2015. Magnetic mineral diagenesis, *Earth Sci. Rev.,* **151,** 1–47.

Roberts, A.P., Heslop, D., Zhao, X. & Pike, C.P., 2014. Understanding fine magnetic particle systemsthrough use of first-order reversal curve diagrams, *Reviews of Geophysics,* **52**(), 557–602.

Roberts, A.P., Pike, C.R. & Verosub, K.L., 2000. First-order reversal curve diagrams: a new tool for characterizing the magnetic properties of natural samples, *J. geophys. Res.,* **105,** 28 461–28 475.

Rochette, P. & Fillion, G., 1989. Field and temperature behavior of remanence in synthetic goethite: paleomagnetic implications, *Geophys. Res. Lett.,* **16,** 851–854.

Rowland, S.J. & Revill, A.T., 1995. Chromatography in petroleum geochemistry, *J. Chromatogr. Library,* **56,** 127–141.

Schwarz, E.J. & Vaughan, D.J., 1972. Magnetic phase relations of pyrrhotite, *J. Geomag. Geoelect.,* **24,** 441–458.

Sprain, C.J., Feinberg, J.M., Renne, P.R. & Jackson, M., 2016. Importance of titanohematite in detrital remanent magnetizations of strata spanning the Cretaceous-Paleogene boundary, Hell Creek region, Montana, *Geochem. Geophys. Geosyst.,* **17,** 660–678.

Valdez-Grijalva, M.A. & Muxworthy, A.R., 2019. First-order reversal curve (FORC) diagrams of nanomagnets with cubic magnetocrystalline anisotropy: a numerical approach, *J. Magn. Magn. Mater.,* **471,** 359–364.

Valdez-Grijalva, M.A., Muxworthy, A.R., Williams, W., Ó Conbhuí, P., Nagy, L., Roberts, A.P. & Heslop, D., 2018. Magnetic vortex effects on first-order reversal curve (FORC) diagrams for greigite dispersions, *Earth planet. Sci Lett.,* **501,** 103–111.

Verwey, E.J.W., 1939. Electronic conduction of magnetite (Fe3O4) and its transition point at low temperatures, *Nature,* **144,** 327.

Volkman, J.K., Alexander, R., Kagi, R.I. & Woodhouse, G.W., 1983. Demethylated hopanes in crude oils and their applications in petroleum geochemistry, *Geochim. Cosmochim. Acta,* **47,** 785–794.

Wenger, L.M., Davis, C.L. & Isaksen, G.H., 2002. Multiple controls on petroleum biodegradation and impact on oil quality, *Soc. Pet. Eng.,* **5,** 375–383.

Wilkin, R.T. & Barnes, H.L., 1997. Formation processes of framboidal pyrite, *Geochim. Cosmochim. Acta,* **61,** 323–339.